Thermal behavior and thermo-mechanical properties of biocompatible poly(lactic acid)/allyl-POSS nanohybrids

Adriana Nicoleta Frone[1] · Dora Dominica Baciu[2] · Marius Stelian Popa[1] · Cristian Andi Nicolae[1] · Augusta Raluca Gabor[1] · Monica Florentina Raduly[1] · Radu Claudiu Fierascu[1] · Denis Mihaela Panaitescu[1]

Abstract

Polysilsesquioxanes are extensively studied as durable and anti-adherent coatings for medical devices due to their super-hydrophobic properties. However, their particular influence on the thermo-mechanical properties and biocompatibility of poly(lactic acid) (PLA)-based materials obtained by melt compounding is scarce. Herein, a facile and promising method to improve the performances of PLA for biomedical applications via the incorporation of different mass proportions of POSS nanoparticles with allyl-heptaisobutyl (AH-POSS) substituent through a melt-blending technique is proposed. The thermal, morpho-structural, mechanical properties at room (RT) and body temperatures (BT), and *in vitro* biocompatibility of the developed PLA/AH-POSS nanohybrids were investigated. AH-POSS nanoparticles were found to have simultaneous nucleation and plasticizing effects on the PLA nanohybrids, inducing enhanced thermal resistance and easy control of crystallinity while preserving PLA's biocompatibility. An interesting effect of AH-POSS on the mechanical properties of PLA at body temperature was observed. These results indicate the considerable potential of the PLA/AH-POSS nanohybrids obtained by melt compounding in the fabrication of biomedical devices.

Introduction

The excessive consumption of goods that has been governing our society for decades led to serious problems such as the depletion of oil reserves and environmental pollution [1]. Therefore, there has been a great deal of motivation for scientists and industries to study and develop biodegradable materials as an alternative to conventional plastics [2]. Nowadays, poly(lactic acid) (PLA) is one of the most important industrial biopolymers due to its mass production from renewable resources such as corn starch, sugarcane or sugar beets [3-5]. It presents good processability, thermal, and mechanical properties, along with a lower price as compared to other biopolymers. Due to its biocompatibility and lack of toxicity, PLA can be used in biomedical applications like tissue engineering, drug delivery systems, orthopedic devices, surgical sutures, or pharmaceutical packaging. However, its brittleness, low crystallization rate, and moisture sensitivity significantly limit its use in a wide range of applications [6, 7]. Several strategies like plasticization, copolymerization, melt blending with other polymers, and the addition of different fillers have been proposed to solve these issues [3, 4, 7-13].

Polyhedral oligomeric silsesquioxanes (POSS) are a class of three-dimensional organic–inorganic hybrid silicon–oxygen nanoparticles with the general formula $(RSiO_{1.5})_n$, whose utility as fillers in different polymeric systems knows a continuous increasing trend [14-20]. The lack of toxicity and no release of volatile organic components along with the presence of cytocompatible moieties make POSS molecules ideal candidates for biomedical and engineering applications [21]. POSS molecules have a Si–O– cage-like structure with organic side groups (alkyl, aryl, or any of

✉ Adriana Nicoleta Frone
adriana.frone@icechim.ro

1 National Institute for Research & Development in Chemistry and Petrochemistry - ICECHIM, 202 Splaiul Independentei, 060021 Bucharest, Romania

2 Cantacuzino National Medical-Military Institute for Research and Development, 103 Spl. Independentei, 050096 Bucharest, Romania

their derivatives) linked to the silicon atoms by covalent bonds [19]. The organic moieties ensure the compatibility between POSS and the polymeric matrix, their solubility and reactivity whereas the inorganic structure provides increased thermal stability and mechanical properties along with a better flame resistance [22, 23]. POSS nanoparticles can be incorporated into the polymer matrix by physical blending or chemical reactions but achieving a controlled nanostructure and a good dispersion of the nanoparticles into the polymer matrix remains an open challenge [15, 18].

The use of PLA-based biomaterials in the medical field has seen remarkable growth especially in wound dressing and tissue engineering [24, 25]. In several biomedical applications, anti-adherent properties are desired. In particular, such biomaterials are needed in hernia repair to avoid peritoneal adhesions after surgical interventions [24, 26]. Polysilsesquioxanes are extensively studied for durable and anti-adherent coatings for medical devices due to their superhydrophobic properties [27, 28]. However, a limited number of studies regarding the effect of POSS on the mechanical and thermal properties of PLA and scarce results on the surface chemical properties and biocompatibility of such hybrid materials were found in the literature [3, 17, 22]. Rezaei et al. compared the influence of trifluoropropyl POSS and titanium dioxide on the morphology, rheology, and crystallization of PLA-based nanocomposites prepared via solution casting [5]. They found that POSS had a better distribution within the PLA matrix compared to TiO_2, and a lubricating effect that caused a boost in PLA crystallinity according to differential scanning calorimetry (DSC) analysis [5]. PLA composites with octaphenyl silsesquioxane (OPS), obtained through extrusion and injection molding, showed flame retardancy properties, which were affected by the degree of crystallinity and crystalline structure of PLA [6]. In particular, a higher PLA crystallinity led to better flame retardancy and mechanical properties for the resulting PLA/OPS composites. The effect of various mass ratios (1, 3, 7, and 10 mass%) of octavinylisobutyl silsesquioxane on the fracture behavior of PLA composites was studied through essential work of fracture (EWF) methodology and the maximum EWF values were obtained for the PLA composite containing 7 mass% POSS [22]. The addition of biodegradable aliphatic poly(carbonate) (PPC) along with polyethylene glycol-polyhedral oligomeric silsesquioxane (PEG-POSS) in PLA and the use of reactive melting extrusion were also proposed for improving the properties of PLA [29]. This route has the advantage of better tailoring the tensile, bending, and impact strength of the obtained composites due to the presence of more components with different properties. A simultaneous improvement in the toughness and strength of PLA was obtained by synthesizing a three-dimensional POSS structure with a Si_8O_{12} core and eight branched PLLA arms, which was added to PLA using a solution casting method [11]. Although complicated due to the synthesis of the POSS modifier, this method ensured the improvement of properties due to the stronger interface between the PLA matrix and POSS nanoparticles [11].

We hypothesize that a better route to improve the properties of PLA films for biomedical applications is the addition of POSS nanoparticles containing a reactive monofunctionality using a melt compounding technique. Melt blending is a preferred route due to the lack of solvents and easy scalability in industrial facilities. The addition of a POSS with an allyl-heptaisobutyl substituent (AH-POSS) may increase the compatibility between PLA and POSS by specific interactions, thus improving nanoparticles' dispersion and, consequently, PLA's properties. Here, the role of AH-POSS in the absence of any compatibilizer on the thermal, mechanical properties, and biocompatibility of PLA/AH-POSS nanohybrids was studied. For the first time, the mechanical properties of PLA/POSS nanohybrids were assessed at body temperature for estimating the mechanical performance of these materials when they are used in vivo. Moreover, this study gives insight into how to tailor the PLA's properties for biomedical applications by changing AH-POSS content and annealing conditions.

Experimental

Materials

Polylactide pellets (PLA – Ingeo™ 4043D grade) with the isomers ratio L/D = 98/2 and a density of 1.24 g cm^{-3} were supplied by Nature Works LLC (USA). The 1-allyl-3,5,7,9,11,13,15-heptaisobutyl-POSS (denoted AH-POSS) with empirical formula $C_{31}H_{68}O_{12}Si_8$, in powder form, showing a density of 1.07 g cm^{-3} and a molecular mass of 857.55 g mol^{-1}, was purchased from Sigma-Aldrich. 3-(4,5-dimethylthiazol-2-yl)-2,5-diphenyltetrazolium bromide (MTT), N–N-dimethylformamide (DMF), sodium dodecyl sulfate (SDS), acetic and hydrochloric acids were supplied by Sigma-Aldrich (USA), fetal bovine serum was obtained from Biochrom AG (Germany), while Dulbecco's modified Eagle's medium (DMEM) and penicillin/streptomycin were purchased from Lonza (Belgium).

Preparation of nanohybrids

The PLA pellets and AH-POSS powder were dried in a vacuum oven at 80 °C for 4 h prior to processing. Afterward, they were melt-mixed in a Brabender LabStation (Germany) equipped with a 30 cm^3 mixing chamber at a temperature of 175 °C and a rotor speed of 75 min^{-1}. AH-POSS was added after PLA melting (about 2 min) and the materials were mixed for another 8 min, the total mixing time being

10 min. The obtained nanocomposites containing 1, 3, 5, and 7 mass% (w/w) AH-POSS were molded into sheets with a thickness of 0.25 ± 0.03 mm through hot pressing (P200E, Dr. Collin, Germany) in the following conditions: temperature of 170 °C, 150 s of preheating at 0.5 MPa and 60 s of compression at 10 MPa, followed by rapid cooling in a cooling cassette. A neat PLA sample was obtained in the same conditions and used as a blank sample. The nanohybrids were denoted as PLA/AHx, with x the concentration of AH-POSS in the samples.

Characterization

Thermal characterization

The thermal decomposition of PLA/AH nanohybrids was investigated by thermal gravimetric analysis (TGA) using a Q5000IR (TA Instruments, USA) analyzer. The measurements were carried out under a N_2 atmosphere at a heating rate of 10 °C min^{-1} from 35 to 700 °C. The sample mass was 5 to 6 mg for each measurement.

The crystallization and melting phenomena were assessed by differential scanning calorimetry (DSC) with a DSC Q2000 calorimeter (TA Instruments, USA). Samples weighing ~ 4 mg were placed in aluminum pans and heated from 5 to 205 °C, held for 2 min to erase the thermal history, then cooled to 5 °C, and again heated to 205 °C at a constant heating–cooling–heating rate of 10 °C min^{-1} under helium flow (25 mL min^{-1}). The melting temperature (T_m) was taken as the peak temperature of the melting endotherm, and the degree of crystallinity (X_c) was calculated from the first heating scan as follows:

$$X_c[\%] = \frac{\Delta H - \Delta H_{cc}}{\Delta H_0 w_{PLA}} \times 100 \qquad (1)$$

where ΔH and ΔH_{cc} are the melting and cold crystallization enthalpies of the nanohybrids, ΔH_0 is the melting enthalpy of 100% crystalline PLA, and w_{PLA} is the mass fraction of PLA in the nanohybrids. ΔH_0 was taken as 93 J g^{-1} [6].

Mechanical tests

Dynamic mechanical analysis (DMA) was conducted in multi-frequency-strain mode using a Q800 analyzer (TA Instruments, USA). Samples with the length × width × thickness of $12 \times 6 \times 0.2$ mm^3 were heated from room temperature to 150 °C with a heating rate of 3 °C min^{-1}.

Tensile tests were carried out on an Instron 3382 Universal Testing Machine using dog-bone shaped specimens according to ISO 527, and three specimens were tested for each sample. A crosshead speed of 2 mm min^{-1} was used for the measurements which took place at room temperature and at 37 °C (body temperature). For the increased temperature, an Instron heating chamber with controlled temperatures in the range from −70 °C to + 250 °C was used. Each specimen was kept in the heating chamber for 5 min before starting the tensile test for ensuring that the temperature of 37 °C was reached throughout the specimen.

Structural analysis

The X-ray diffraction (XRD) patterns for the nanohybrids were recorded with a Rigaku SmartLab diffractometer operated at 45 kV and 200 mA, parallel beam configuration (2θ/θ scan mode), using Cu (Kα) radiation ($\lambda = 1.54059$ Å).

Fourier transform infrared (FTIR) spectroscopic analysis was performed at room temperature on a Jasco FTIR 6300 spectrometer equipped with an ATR Specac Golden Gate accessory (KRS5 lens). Neat PLA and nanohybrids sheets obtained through hot pressing were analyzed as such and after annealing at 90 °C for 60 min followed by slowly cooling until room temperature. FTIR spectra were obtained by accumulating 32 scans per spectrum with a resolution of 4 cm^{-1} in the wavenumber range of 4000–400 cm^{-1}. The background spectrum was collected before each sample.

Atomic force microscopy (AFM)

A MultiMode 8 atomic force microscope from Bruker Nano Inc. (USA) equipped with a Nanoscope V controller and Nanoscope Software version 1.20 was used for the AFM measurements. The images were taken in Peak Force Quantitative Nanomechanical Mapping (PF-QNM) mode in air, using silicon nitride tips, at a constant scan rate of 1.3 Hz and a scan angle of 90°.

Cytotoxicity and cell proliferation studies

The cytotoxic potential of the neat PLA and PLA/AH-POSS nanohybrids was evaluated against L929 murine fibroblast cells type ECACC (European Collection of Authenticated Cell Cultures, England) by LDH assay. All samples were sterilized with 70% ethanol solution and round disk-shaped samples, 10 mm in diameter, were cut from each sample and further sterilized for 15 min using UV irradiation. L929 cells were cultured in DMEM supplemented with 10% fetal bovine serum (FBS, Biochrom AG, Germany) and antibiotics, 100 U mL^{-1} penicillin—100 μg mL^{-1} streptomycin on 75 cm^2 flasks in a humidified atmosphere at 37 °C and 5% CO_2. L929 cells were seeded in 96-well plates, bottom covered by the round disk-shaped nanocomposite samples at a starting density of 10^4 cells/well and grown overnight to allow adherence (100 μL/well) in complete culture medium. Cell viability was measured using the lactate dehydrogenase detection kit (CytoTox 96R, Promega). Briefly, 50 μl culture

mediums from all wells were changed to a fresh 96-well flat-bottom plate and 50 µL CytoTox 96R reagent was added to each sample. The samples were incubated with the reagent at room temperature in the dark for 30 min. LDH concentration was determined by measuring the optic density of the resulting solution at 492 nm within 1 h after adding the stop solution.

The morphology and proliferation of L929 cells cultured on neat PLA and PLA/AH-POSS nanohybrids were investigated by fluorescence microscopy. Each sample with L929 cells, cultured this time in 24-well plates, was washed with phosphate-buffered saline (PBS) and fixed with 2% para-formaldehyde solution (Sigma-Aldrich) for 30 min. After fixation, the samples were stained with 4′,6-diamidino-2-phenylindole (DAPI, Life) for nuclei and Texas-Red-X Phalloidin (Molecular Probes, Thermo Fisher Scientific) for actin filaments. Images were acquired using an Eclipse TE2000 inverted fluorescence microscope (Nikon, Austria) and processed with ImageJ software.

Results and discussion

Thermal stability of PLA/AH-POSS nanohybrids

TGA and derivative (DTG) curves along with the corresponding data for the neat components and the PLA/AH-POSS nanohybrids are shown in Fig. 1a–d and Table 1. The onset degradation temperature (T_{on}), the temperature at 10% mass loss ($T_{10\%}$), and the temperature at maximum mass loss rate (T_{max}), along with the char residue at 600 °C ($R_{600°C}$), were obtained from these curves. AH-POSS showed a two-stage decomposition process, with the major one having a T_{max} at 245 °C and the minor one showing a T'_{max} at 496 °C. In the first decomposition stage, more than 77 mass% of the total mass of AH-POSS was lost up to 260 °C. The T_{on} of AH-POSS was 223 °C; therefore, it was not degraded during the melt-mixing process employed in the preparation of the nanohybrids, which took place at 175 °C. This is also supported by the small mass loss recorded for all nanohybrids at the processing temperature, $WL_{175°C}$ varying between 0.28 and 0.34% (Table 1). The residue $R_{600°C}$ of AH-POSS was 10.81% (Fig. 1a).

Neat PLA started to degrade at 336 °C (T_{on}), showing a T_{max1} at 361 °C, when it lost more than 67% of its mass, and a small shoulder at 435 °C (T_{max2}). According to Fig. 1b, c and Table 1, the addition of AH-POSS induced a delay in the thermal decomposition of PLA matrix in all nanohybrids. Thus, for the PLA/AH nanohybrids with 3–7 mass% AH-POSS, the T_{on} shifted to higher values by about 10 °C and the T_{max1} by 4–5 °C. Moreover, T_{max2} shifted by 50–80 °C in all PLA/AH nanohybrids as compared to neat PLA (Fig. 1d).

It is worth mentioning that, although AH-POSS had poorer thermal stability compared to PLA (Fig. 1a), the PLA/AH nanohybrids exhibited better thermal behavior when exposed to increased temperatures. This behavior could be due to the barrier effect of the AH-POSS nanoparticles and their degradation compounds that limited the heat flux to the PLA matrix and hindered the release of degradation products. A good interaction between the PLA and POSS nanoparticles could also contribute to an improved thermal stability. These findings are in agreement with literature reports on similar nanocomposite systems [3, 11]. Looking at the char residue variation one may observe a continuum increase with the increase in the AH-POSS content (Fig. 1e). However, the theoretical residue values calculated for the nanohybrids by considering the $R_{600°C}$ values for neat PLA and AH-POSS were higher than the experimental ones for a content of AH-POSS of 3 – 7 mass% in the nanohybrids (Fig. 1e). This behavior may be due to the decomposition products of AH-POSS which partially leaves from the residue with the gaseous products [6].

Interestingly, the increase in the characteristic temperatures did not follow the concentration of AH-POSS in the nanohybrids, the maximum values for T_{on}, $T_{10\%}$, and T_{max} being observed for 3 and 5 mass% POSS in the nanohybrids. One cause of this behavior could be the poor dispersion of AH-POSS nanoparticles and the occurrence of agglomerates at higher concentrations (7 mass%) of AH-POSS nanoparticles in PLA. This aspect was verified by the AFM morphological investigation of the PLA/AH-POSS nanohybrids (Fig. 2).

Figure 2 shows the AFM Peak force error (PFE) images of neat PLA and nanohybrids with 1, 3, 5 and 7 mass% AH-POSS. The AH-POSS nanoparticles appeared on the surface of the nanohybrids as well-defined formations, lighter in color than the PLA matrix due to the difference in densities. An agglomeration tendency was observed at a higher amount of AH-POSS in nanohybrids (PLA/AH5 and PLA/AH7), similar to other observations on polymer/POSS hybrids [30]. Moreover, a poor distribution of AH-POSS was also noticed in PLA/AH7 nanohybrids, where areas with agglomerated nanoparticles are separated by areas without nanoparticles (Fig. 2). Remarkably, these AH-POSS formations have an elongated form, with a width varying between 20 and 60 nm and a length between 100 and 500 nm. A similar elongated morphology of POSS aggregates in the form of elongated formations was reported by Soong et al. for plasticized PVC/POSS hybrids [30]. Furthermore, in the magnified inset PFE images, one can observe that the AH-POSS nanoparticles are covered by a polymer layer. Along with the tip widening effect characteristic to AFM imaging of nanostructures [31], this polymer covering made difficult an accurate determination of the dimensions of the AH-POSS structures; however,
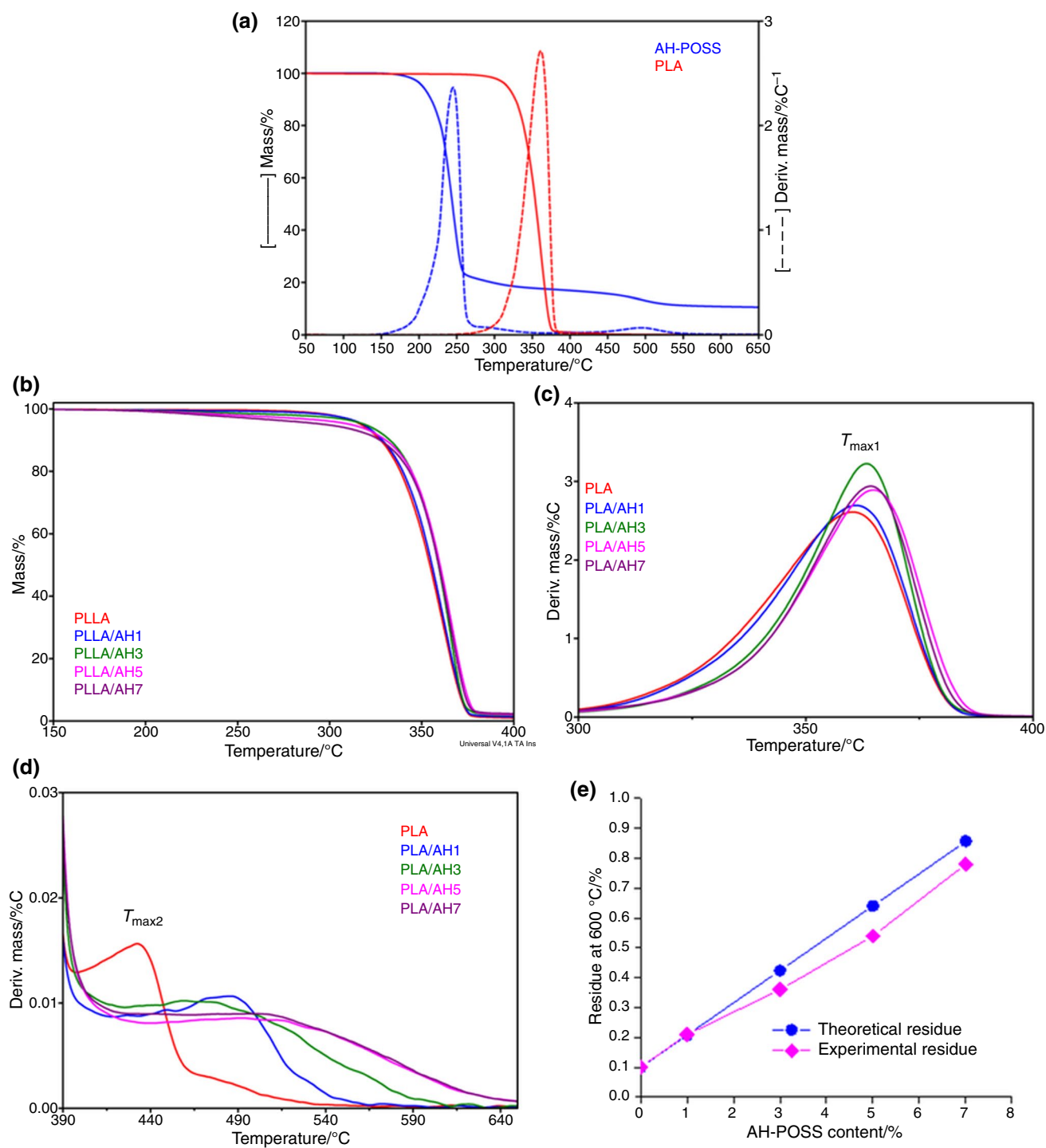
Fig. 1 TGA and DTG curves for **a** neat PLA and AH-POSS, and **b**, **c** PLA/AH-POSS nanohybrids; **d** DTG curves in the range 400–650 °C; **e** theoretical and experimental residue at 600 °C

this also showed a good interfacial adhesion between the AH-POSS and PLA matrix.

FTIR spectroscopy

FTIR spectra of neat PLA and AH-POSS along with those of nanohybrids are shown in Fig. 3. AH-POSS showed a strong peak at 1085 cm^{-1} with a shoulder at 1037 cm^{-1}

Table 1 TGA data for neat PLA and PLA/AH nanohybrids

Sample	$T_{on}/°C$	$T_{10\%}/°C$	$WL_{175°C}/°C$	$T_{max1}/°C$	$T_{max2}/°C$	$R_{600°C}/°C$
PLA	335.9	327.6	0.21	361.2	435.4	0.10
PLA/AH1	338.4	328.6	0.28	361.8	488.2	0.21
PLA/AH3	346.0	332.7	0.29	365.2	498.9	0.36
PLA/AH5	345.1	330.5	0.31	366.0	517.0	0.54
PLA/AH7	343.9	327.3	0.34	365.8	515.8	0.78

Fig. 2 PFE images of PLA nanohybrids with different AH-POSS loadings
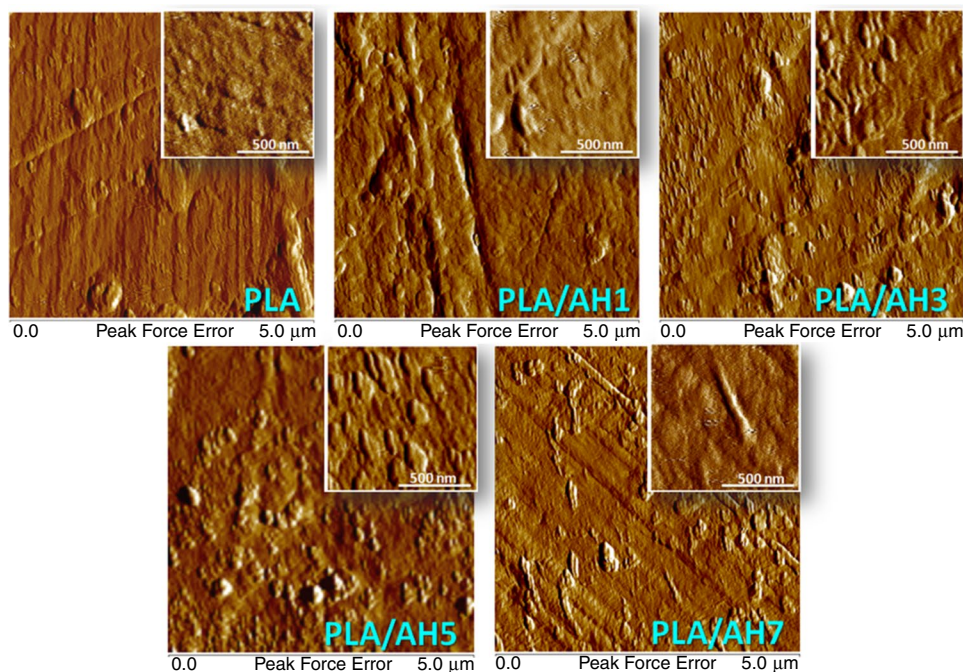
corresponding to the asymmetric and symmetric stretching vibrations of Si–O–Si in the silsesquioxane cage [32, 33], characteristic peaks at 1229 and 899 cm^{-1} (Si–C stretching) [32, 34, 35], 837 and 745 cm^{-1} (Si–C wagging) [32, 35], and a well-defined peak centered at 1635 cm^{-1} resulting from the vibration of the allyl double bond of the functional group (Fig. 3b) [36]. The C–H stretching and deformation vibrations of the isobutyl substituents of AH-POSS were observed at 2953/2871 cm^{-1} and 1464/1367 cm^{-1}, respectively [35, 37].

All nanohybrids displayed similar peaks to those characteristic of PLA (Fig. 3a) at 2995/2945 and 2880 cm^{-1} due to CH$_3$ asymmetric/symmetric stretching vibration and CH stretching, respectively [6, 38], 1749 cm^{-1} corresponding to the C=O stretching vibration of carbonyl group [38, 39], 1453, 1382 and 1360 cm^{-1} due to C–H deformation in CH$_3$ and CH [6, 38], 1266, 1180 and 1080 cm^{-1} corresponding to the asymmetric and symmetric stretching vibration of C–O bond in the C–O–C group [39, 40], and at 1043 cm^{-1} due to C–CH$_3$ symmetrical stretching [38, 39]. It is worth mentioning that the peak corresponding to the C=O stretching vibration from 1749 cm^{-1} corresponds to the amorphous

PLA. Nevertheless, the signal attributed to the allyl double bond in the AH-POSS structure from 1635 cm^{-1} was not visible in the PLA/AH-POSS nanohybrids (Fig. 3c). Therefore, it may be supposed that the allyl groups were consumed in the coupling of AH-POSS with the polymeric matrix at elevated temperatures and under mechanical stress, which are characteristic to the melt processing of nanohybrids. Furthermore, it can be seen that the intensity of the C=O bonds at 1749 cm^{-1} [38, 39] decreased in the nanohybrids with 1 and 3 mass% POSS due to the possible participation of this bond in the chemical reaction with the allyl group. A schematic representation of a possible chemical linkage between PLA and AH-POSS is presented in Fig. 4.

Calorimetric analysis of PLA/AH-POSS nanohybrids

The DSC curves of neat PLA and PLA/AH nanohybrids corresponding to the first heating and cooling scans are illustrated in Fig. 5a. The typical calorimetric data, including the degree of crystallinity, glass transition of PLA (T_g), cold crystallization (T_{cc}), and melting temperatures along with
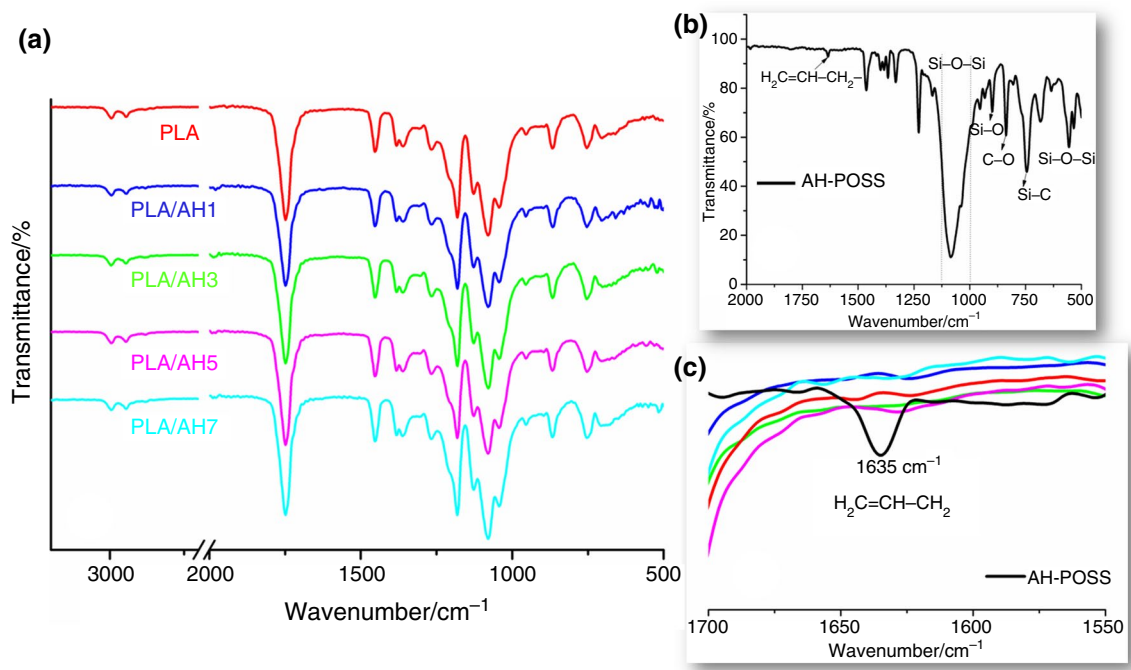
Fig. 3 ATR-FTIR spectra for **a** neat PLA and PLA/AH-POSS nanohybrids, **b** neat AH-POSS, and **c**, color of the curves identical to those from Fig. 3a) inset of enlargement in the range 1700–1550 cm^{-1}
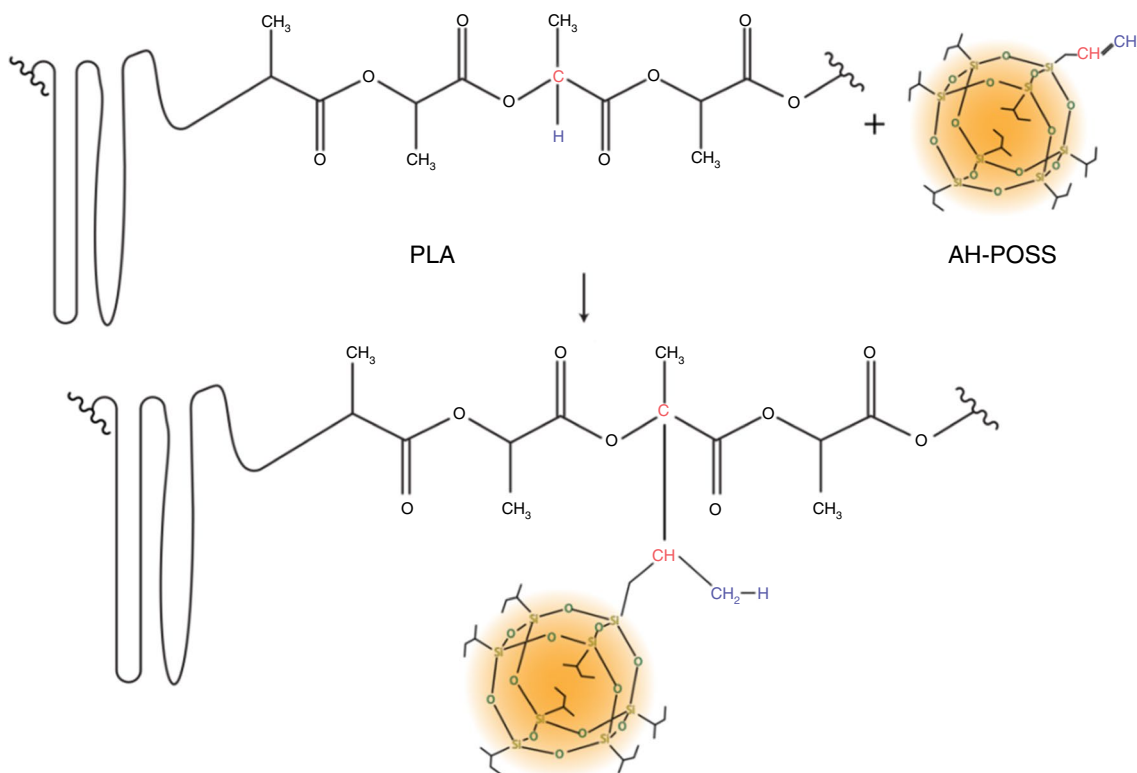

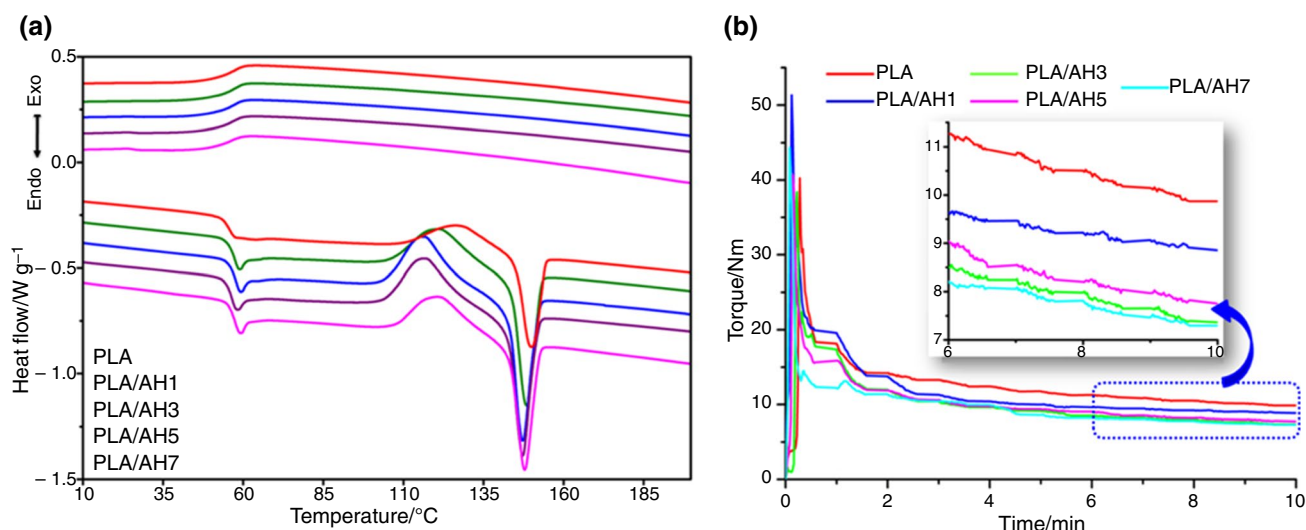**Fig. 4** Schematic representation of possible chemical linkage between PLA and AH-POSS nanoparticles

Fig. 5 **a** DSC first heating and cooling curves and **b** melt torque vs. blending time for neat PLA and PLA/AH-POSS nanohybrids

Table 2 DSC results determined from the first heating scan for neat PLA and PLA/AH-POSS nanohybrids

Sample	T_g/°C	T_{cc}/°C	ΔH_{cc}/J g^{-1}	T_m/°C	ΔH_m/J g^{-1}	X_c/%
PLA	56.3	126.3	9.4	149.7	18.3	9.6
PLA/AH1	57.3	120.8	15.7	148.4	25.6	10.8
PLA/AH3	58.0	116.4	18.3	147.3	28.8	11.6
PLA/AH5	56.7	116.7	16.8	147.2	28.1	12.8
PLA/AH7	57.6	120.5	12.7	147.8	25.2	14.5

the enthalpies of cold crystallization (ΔH_{cc}) and melting (ΔH_m) processes, are collected in Table 2.

The addition of AH-POSS had a low influence on the T_g value of the neat PLA, with all the nanohybrids showing a T_g between 56 and 58 °C, similar to that of PLA (56 °C) (Fig. 5a, Table 2). A noticeable difference between neat PLA and nanohybrids is the presence of a small endotherm that overlapped the glass transition only for nanohybrids (Fig. 5a). This endothermic event that occurred at the higher temperature side of the T_g signal is generally ascribed to the relaxation of the ordered polymer chains resulted from the processing step [41]. This enthalpy recovery peak was also observed in PLA nanohybrids with cellulose fibers and it appeared more prominent in nanohybrids compared to neat PLA [42].

The weak effect of the AH-POSS on the T_g of PLA suggests a small influence of the AH-POSS on the mobility of PLA chains and questions the existence of interactions between the two components. On the contrary, the enthalpy relaxation observed only in nanohybrids highlights a strong influence of the AH-POSS on the organization of PLA in the glassy state, in particular on its orientational order [43]. In addition, the presence of bonds between AH-POSS and PLA in nanohybrids could also lead to a more stable phase

and, therefore, to an enthalpy relaxation during glass transition [43]. These results which seem contradictory suggest the influence of more factors on the thermal behavior of nanohybrids. The analysis of the melt viscosity during the melt-mixing process showed lower torque values in the case of nanohybrids compared to neat PLA (Fig. 5b). Therefore, AH-POSS also had a plasticizing effect, similar to other POSS modifiers [3]. This effect could overlap with the reduced mobility caused by the AH-POSS-PLA interactions, leading to small or no variation in the T_g value, as observed in the case of nanohybrids (Table. 2). This plasticizing role of AH-POSS nanoparticles is very important for the further processing of these materials through 3D printing for obtaining medical devices.

During heating, all PLA nanohybrids started to crystallize from a lower temperature with up to 10 °C than the neat PLA and showed increased ΔH_{cc} values with up to 100%, showing the nucleating effect of the AH-POSS nanoparticles (Table 2). The nanohybrids containing 3 and 5 mass% AH-POSS showed the highest crystallization ability i.e. the lowest T_{cc} and the highest ΔH_{cc} values (Table 2, Fig. 5a). Otherwise, the incorporation of AH-POSS in PLA had almost no influence on the melting temperature of PLA (Table 2); however, the melting endotherms of nanohybrids were larger

and sharper compared to that of PLA (Fig. 5a), showing the ability of AH-POSS to enhance PLA's crystallization [42]. The effect of the AH-POSS nanoparticles was important, leading to a continuous increase in the PLA's crystallinity by 20–50% with the increase in their concentration in nanohybrids from 3 to 7 mass% (Table 2). An increase in crystallinity of only 4% was reported for the PLA composites with 10 mass% OPS type POSS particles [6].

XRD analysis

The crystalline structure and crystallinity of PLA matrix, AH-POSS nanoparticles and nanohybrids were studied by XRD (Fig. 6a).

The patterns of AH-POSS nanoparticles revealed a specific rhombohedral crystal profile with strong crystalline peaks at $2\theta = 8.00°$, $8.81°$, $10.85°$, $11.72°$, $18.49°$, $19.22°$ and $19.86°$ corresponding to a d-spacing of 11.04, 10.02, 8.14, 7.54, 4.79, 4.61 and 4.46 Å, respectively. The peak at $2\theta = 8.00°$ with a d-spacing of 11.04 Å is determined by the size of the heptaisobutyl POSS molecules [44]. The XRD pattern of neat PLA contains only a broad hallow at $2\theta \sim 15°$, which corresponds to the amorphous PLA, also observed in the FTIR spectra. Therefore, the crystallinity of the PLA film obtained by compression molding and rapid cooling was too small to be detected by the XRD analysis.

The XRD patterns of the nanohybrids (Fig. 6a) displayed similar amorphous hallows as neat PLA and the reflections characteristic to the AH-POSS crystals, whose intensity increased with the increase in nanoparticles content. This may indicate that the POSS moieties were chemically linked to PLA according to a previously published report [37].

Interestingly, the crystalline structure of PLA and nanohybrids was not revealed by XRD or FTIR measurements, probably due to the slow crystallization of PLA in the absence of additional treatments [45], as also observed from the lack of a crystallization event in the DSC cooling scan (Fig. 5a). Moreover, the AFM investigation of PLA and nanohybrids revealed a typical amorphous structure free of visible formations or defects in the PFE images from Fig. 2. Therefore, the PLA and nanohybrids films were thermally treated in order to enhance the crystallization capacity of PLA by annealing in an oven at 90 °C for 60 min followed by slowly cooling until room temperature. The films were characterized after annealing by XRD, AFM, and FTIR.

Crystalline structure and morphology of PLA and nanohybrids after annealing

The XRD patterns of the annealed samples (Fig. 6b) showed the characteristic peaks of the α-form of PLA at $2\theta = 14.8$, 16.6, 19.1° and 22.3° consistent with previously published data [6, 11]. These peaks correspond to the (010), (200)/(110), (203) and (015) planes of the orthorhombic crystal lattice of PLA [46, 47]. Therefore, the incorporation of AH-POSS did not influence the crystalline structure of PLA. However, the XRD peaks at 8.1–8.2°, belonging to the crystalline structure of AH-POSS, increased linearly in intensity with the increase in the AH-POSS content in the nanohybrids.

AFM topographic and PFE images of PLA and PLA-AH7 annealed for 60 min at 90 °C are shown in Fig. 7. The images illustrate the formation of thin lamellae which have grown along random axes similar to leaf veins. The lamellae thickness was found to be 10–20 nm for both samples,
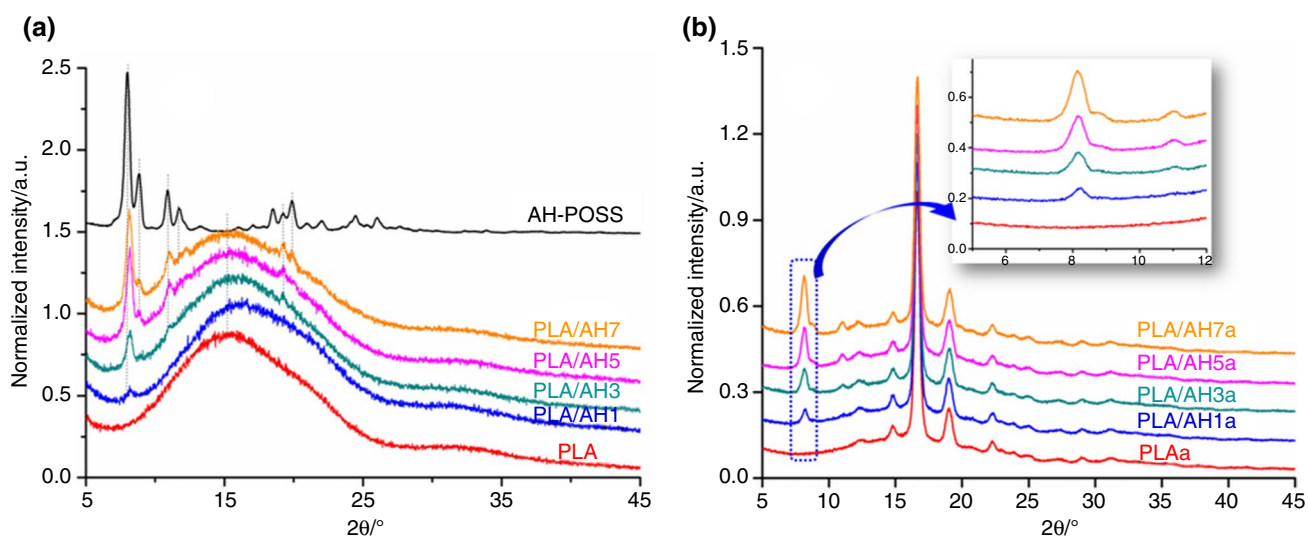

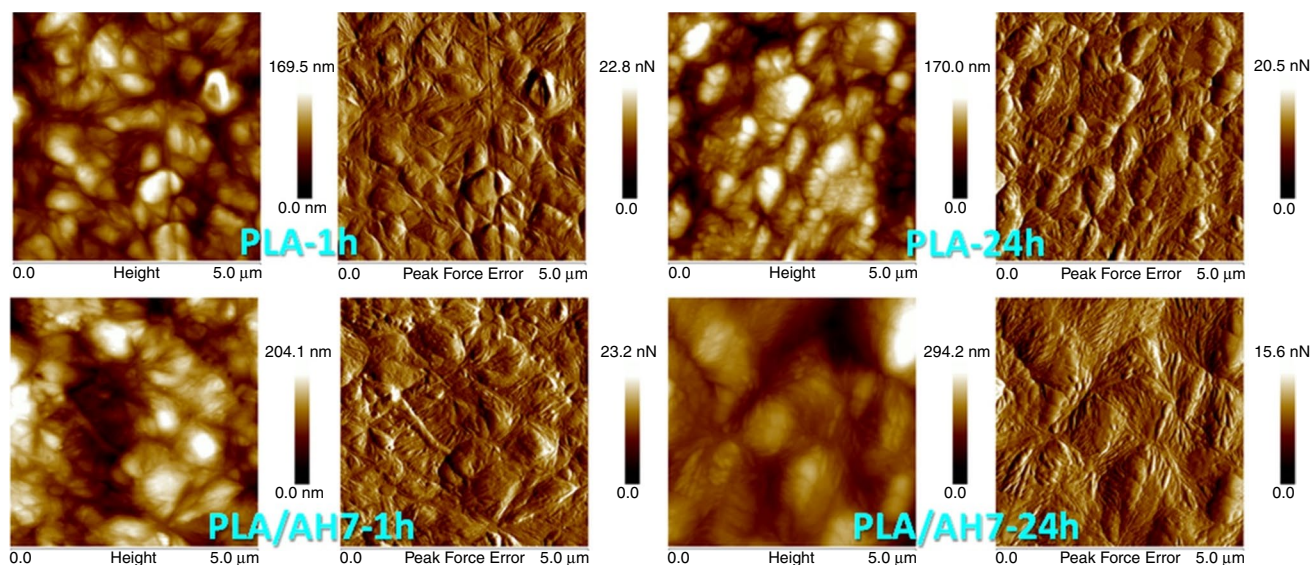**Fig. 6** XRD patterns of neat PLA, AH-POSS and nanohybrids **a** before and **b** after annealing

Fig. 7 AFM topographics and PFE images of PLA and PLA-AH7 annealed at 90 °C for 60 min and 24 h

while the space between crystalline lamellae was 10–15 nm. A clearer lamellar structure was observed in the nanohybrids compared to neat PLA. This highlights the favorable effect of the AH-POSS on the crystallization of PLA, also noticed by DSC. However, the AH-POSS presence on the surface of PLA/AH7 nanohybrids was hardly detected: the few objects that can be ascribed to the AH-POSS nanoparticles or their agglomerates were covered by a layer of well-structured polymer matrix (Fig. 7). Increasing the annealing time to 24 h has the effect of enhancing the crystallization of both samples. A spherulitic morphology with lamellar structures of more uniform shape and size was observed in the case of PLA/AH7, which highlights the nucleation effect

of the siloxane networks upon PLA crystallization. Lamellar stacks with almost parallel lamellae are frequently observed in Fig. 7 (PLA/AH7-24 h). On the contrary, lamellar bundles aggregated into different geometric shapes with a shorter distance order were noticed in the neat PLA sample (Fig. 7: PLA-24 h).

The crystallization of PLA and nanohybrids after annealing was also highlighted in the FTIR spectra, especially in the region from 1500 to 800 cm^{-1}, which is sensitive to the PLA crystallization [48] (Fig. 8). After annealing, a new band appeared at 921 cm^{-1} in the spectra of PLA and PLA/AH7, which is characteristic of PLA α-form crystals. Similarly, the intensity of the bands from
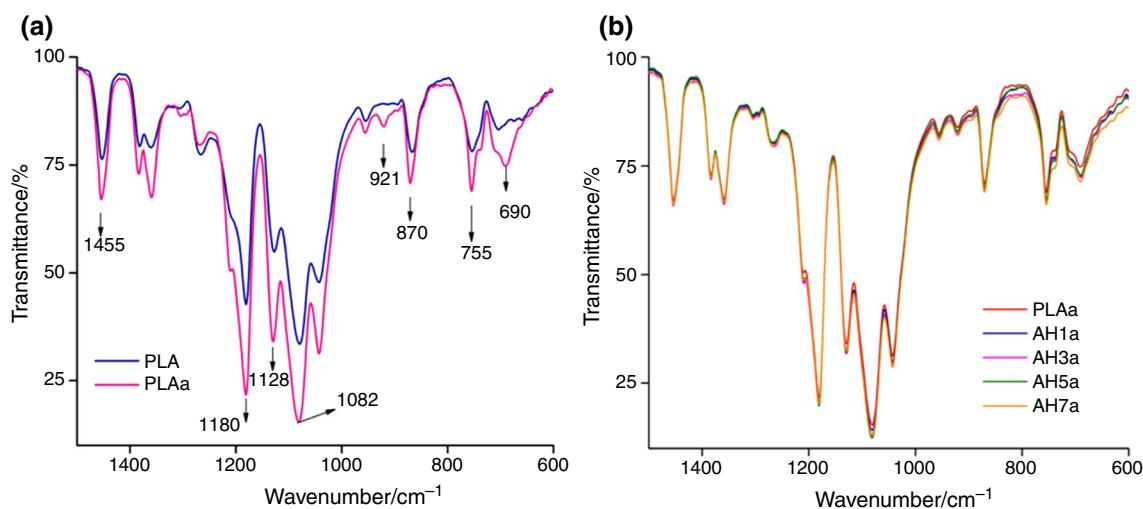

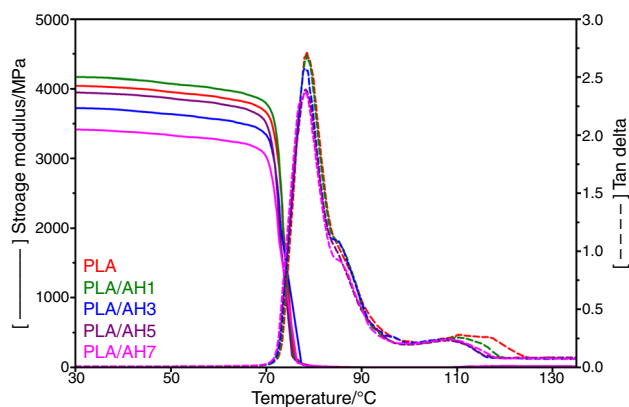**Fig. 8** ATR-FTIR spectra of **a** neat PLA and **b** PLA-AH7 after annealing

Fig. 9 E' and tan δ as a function of temperature for neat PLA and PLA/POSS nanohybrids

Table 3 DMA data for neat PLA and PLA/AH-POSS nanohybrids

Sample	E'/MPa		$T_g{}^*$/°C	$T_{cc}{}^*$/°C
	E'_{30}	E'_{80}		
PLA	4045	19.82	78.49	116.8
PLA/AH1	4167	20.42	78.55	110.5
PLA/AH3	3725	18.59	78.35	108.5
PLA/AH5	3950	22.09	78.41	108.8
PLA/AH7	3417	20.23	78.24	108.7

$^*T_g$, T_{cc} determined from DMA

870 to 755 cm^{-1}, corresponding to the vibration of C–COO bond in the crystalline phase of PLA, was enhanced in PLA and nanocomposite after annealing (Fig. 8).

DMA analysis of PLA/AH-POSS nanohybrids

The storage modulus (E') and tan δ of neat PLA and PLA/POSS nanohybrids as a function of temperature are presented in Fig. 9. At temperatures below 60 °C, associated with the PLA's glassy region, higher E' values were obtained only for the PLA nanohybrid containing 1 mass% AH-POSS nanoparticles, the E' values decreasing with the increase in AH-POSS content from 3 to 7 mass% (Fig. 9, Table 3). The decrease in the storage modulus of the nanohybrids compared to neat PLA shows an increase in the PLA's flexibility imparted by the AH-POSS presence, therefore a plasticizing effect. This was pointed out by the decrease in the torque values with the increase in the AH-POSS concentration in nanohybrids (Fig. 5b) and previously reported for other polymer/POSS systems [3, 5].

At temperatures above 60 °C, the E' values of all nanohybrids were similar to or higher than that of neat PLA (Table 3). A slight increase in the E' value was noticed at temperatures above 100 °C for all the samples as a result

of the cold crystallization phenomenon, also observed by DSC. Moreover, the cold crystallization temperature of PLA was seen at lower values in all PLA/AH nanohybrids compared to neat PLA, in good agreement with the previous DSC results. No obvious change in the tan δ peak, showing the $T_{g(DMA)}$ of PLA, was noticed for nanohybrids and neat PLA, which is consistent with the results obtained by DSC regarding the influence of AH-POSS nanoparticles upon the glass transition of PLA (Table 2, Fig. 5a).

Surprisingly, a small but almost gradual downward shift in the tan δ peak intensity was observed with increasing the content of AH-POSS in nanohybrids (Fig. 9). This suggests decreased chain mobility in the amorphous phase of PLA [49], which may result from an increase in the crystalline content or from enhanced interactions between the components. Indeed, a higher crystallinity was obtained by DSC for nanohybrids compared to neat PLA with the increase in the AH-POSS content. In this case, the crystal formation confined the segmental motion of the PLA chains in the amorphous regions, which further led to a lower tan δ peak (Fig. 9) [50]. Moreover, possible chemical linkage between AH-POSS and PLA was highlighted by FTIR and the occurrence of interactions between the components was supported by the TGA, DSC, and AFM results.

Effect of AH-POSS on the mechanical properties of PLA at body temperature

The stress–strain curves of PLA, PLA/AH3, and PLA/AH7 nanohybrids measured at room and body temperatures are shown in Fig. 10a. At room temperature, PLA and nanohybrids showed similar mechanical properties, a tensile strength at break of 25–27 MPa and a very low elongation at break, of 2–4%, which emphasized their high brittleness. Both PLA and nanohybrids fractured in a fully brittle manner without yielding (Fig. 10a). A completely different behavior was observed at body temperature. All the samples showed yielding and a cold drawing plateau which is associated with necking propagation, as observed in Fig. 10b. No strain-hardening was observed and the specimens fractured during necking (Fig. 10a). It is well known that PLA can be easily stretched and is able of large deformation at temperatures close to T_g [51]. Chen et al. studied the mechanical properties of uniaxially pre-stretched PLA correlated with microstructural changes and proposed the mechanisms which determined the ductile behavior of PLA during the tensile test [52]. Thus, after pre-stretching around T_g, the network structure of cohesional entanglements, characteristic to the undrawn PLA, was destroyed because of disentanglements, which promoted the mobility of the PLA molecular chains and the ductile behavior of PLA [52]. They supposed that the orientation of the molecular chains and the occurrence of mesophase during the tensile test might
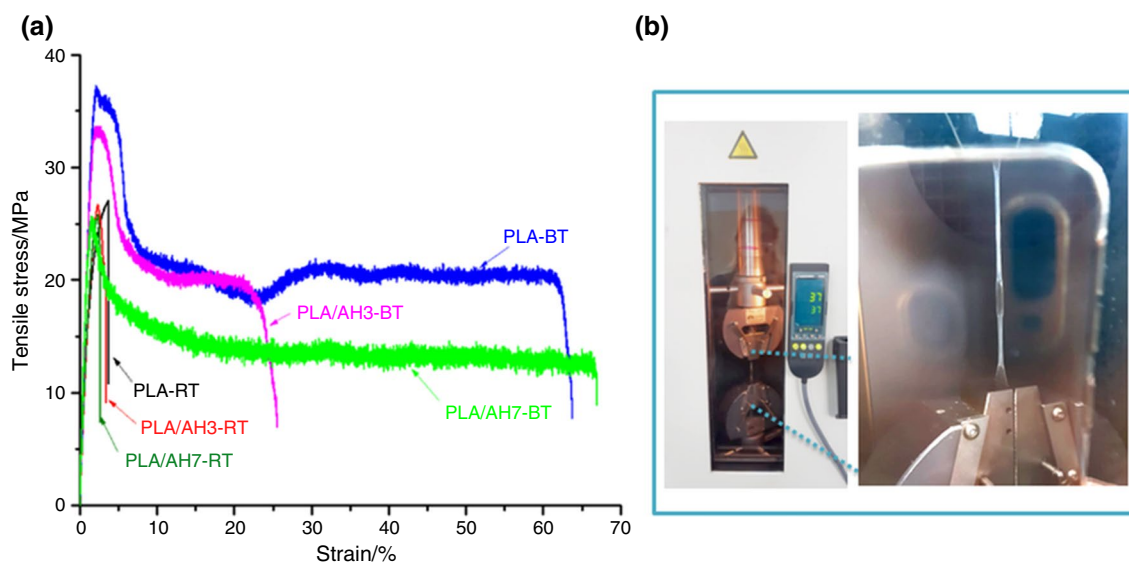
Fig. 10 **a** Stress–strain curves of PLA and nanohybrids with 3 and 7 mass% AH-POSS at 23 °C (RT) and 37 °C (BT) and **b** the elongation of a PLA specimen in the heating chamber at 37 °C showing neck formation and cold drawing in the magnified image

become stress concentration sites leading to fracture. In the case of microporous PLLA, it was observed that shear yielding prevailed over the interfacial debonding mechanisms during the tensile tests at elevated temperatures (50–70 °C) [53]. However, the body temperature in our tests was more than 20 °C below the T_g of PLA and the T/T_g ratio was lower than 0.65. Previous studies on the mechanical behavior of polymethyl methacrylate in uniaxial tensile tests at different temperatures have shown an almost linear stress–strain response and brittle fracture for $T/T_g < 0.8$, similar to that observed for PLA and nanohybrids at RM, and yielding along with neck propagation at T/T_g ratios between 0.8 and 1 [54]. The different behavior of PLA and its nanohybrids might be determined by the temperature raise generated during the deformation of the specimens. Indeed, the strain energy is converted into heat due to the viscous nature of the polymer and hybrids [55]. Due to the poor thermal conductivity of polymers, the local increase in temperature could be important. An increase in temperature of about 10 °C was reported for a polyamide-66 composite reinforced with 30 mass% glass fibers during the fatigue test [55]. However, no information on the temperature raise in PLA during any mechanical test was found in the literature and the mechanisms which determined the ductile behavior of both PLA and nanohybrids during the tensile test remain an open issue to be clarified.

The stress–strain curves of PLA and nanohybrids with 3 and 7 mass% AH-POSS recorded at BT showed that the cold drawing plateau exhibited different lengths depending on the concentration of AH-POSS: higher for PLA and PLA/AH7, and smaller for PLA/AH3. Moreover, different yield strength values were noticed: 37 MPa for PLA, 33 MPa for

PLA/AH3, and only 25 MPa for PLA/AH7. Therefore, the AH-POSS nanoparticles acted as plasticizers increasing the flexibility and also as stress concentrators initiating the breakage. It is worth mentioning that the determination of the mechanical properties at the body temperature is very important because it showed a ductile behavior instead of a brittle one for both PLA and nanohybrids. This may also change the strategy in the design of PLA-based nanocomposites for biomedical applications.

Cytotoxicity and cell proliferation evaluation

The release of LDH in the culture medium of the L929 cells, grown at the surface of the prepared nanohybrids, was used for evaluating their cytotoxicity (Fig. 11a). The quantitative evaluation of materials cytotoxicity by LDH assay showed that after 1 day of exposure, there was a negligible difference in the levels of LDH released in the culture media for control cells compared with cells put in contact with the nanohybrid samples. The statistical evaluation done by Student's t test showed statistically non-significant differences ($p > 0.2$) between the control and the tested samples. These results suggest that both neat PLA and PLA/POSS-AH nanohybrids do not exert cytotoxic effects on murine fibroblasts cell line.

The morphology and proliferation of the adhered cells on the neat PLA and PLA/AH nanohybrids surface are displayed in Fig. 11b. Early proliferation was noticed after only one day incubation, the surface of all the samples being completely covered by L929 cells having their characteristic spindle-shape morphology. The results demonstrate the ability of neat PLA and PLA/AH nanohybrids to promote cell proliferation and allow cell adherence. This is a very
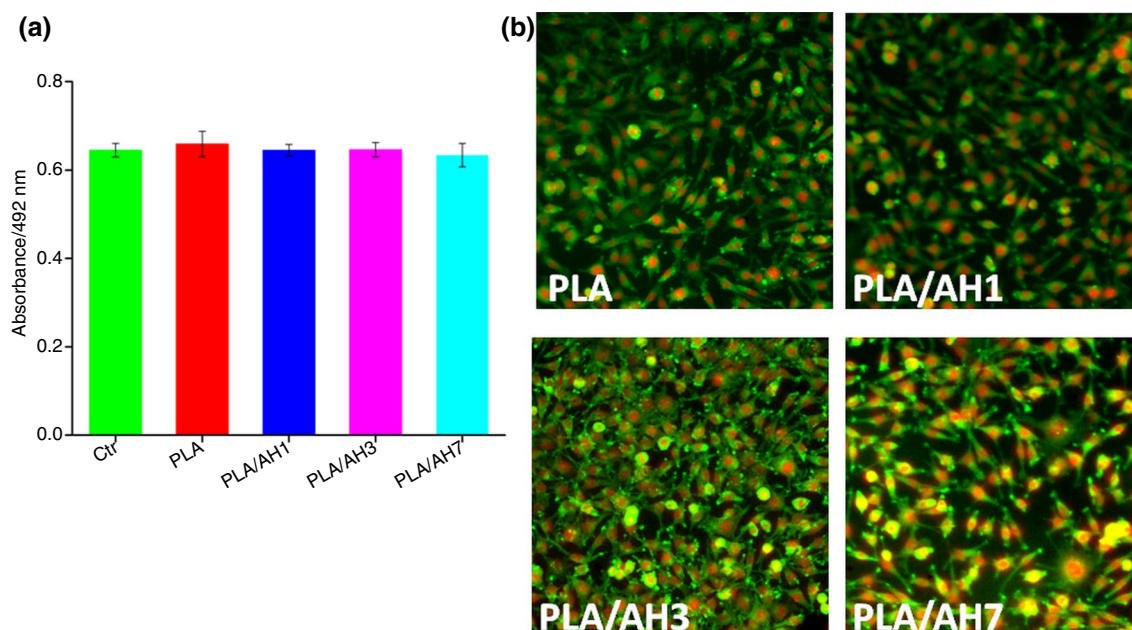
(a)

(b)

Fig. 11 a Cytotoxicity and **b** morphology of L929 cells cultured on neat PLA and PLA/POSS-AH nanohybrids film surfaces

important result because AH-POSS is a hydrophobic additive which may increase the hydrophobicity of the matrix and may lead to reduced cells' adhesion [56]. Indeed, the water contact angle of the films increased from 75° for PLA, to almost 100° for PLA/AH7 nanohybrid, as expected. However, the increased hydrophobicity did not influence cells' proliferation due to the lack of toxicity of AH-POSS.

Conclusions

In this study, a facile and easy scalable method was proposed for improving PLA's properties toward biomedical applications through the addition of different ratios of polyhedral oligomeric silsesquioxane with isobutyl substituent via melt blending. It was found that AH-POSS addition induced a delay in the PLA's thermal decomposition with about 10 °C in nanohybrids with a content of AH-POSS of 3 mass% or more. AH-POSS nanoparticles exhibited both nucleation and plasticizing effects on PLA since an important increase in crystallinity by up to 50% was observed for the nanohybrids as well as lower melt torque values as compared to neat PLA. Furthermore, the as-prepared PLA/AH-POSS nanohybrids have tunable morpho-structural properties by varying the AH-POSS content and annealing conditions as seen from AFM, XRD and FTIR results. The determination of the mechanical properties at body temperature has shown a ductile behavior for both PLA and nanohybrids and not a brittle one, as usually observed after testing at room temperature. Therefore, the mechanical properties at body temperature

are more suitable for the characterization of biomaterials intended for biomedical applications. Cytotoxicity and cell proliferation evaluation results confirmed the suitability of the developed PLA/POSS-AH nanohybrids for the biomedical field due to their ability to promote cell proliferation and cell adherence and the lack of cytotoxic effects.

Declarations

References

1. He L, Song F, Guo ZW, Zhao X, Yang N, Wang XL. Toward strong and super-toughened PLA via incorporating a novel fully bio-based copolyester containing cyclic sugar. Compos Part B: Eng. 2021;207:108558.
2. Inácio EM, Lima MCP, Souza DHS, Sirelli L, Dias ML. Crystallization, thermal and mechanical behavior of oligosebacate plasticized poly(lactic acid) films. Polímeros. 2018;28(5):381–8.

3. Sirin H, Kodal M, Ozkoc G. The influence of POSS type on the-properties of PLA. PolymCompos. 2016;37:1497–506.

4. Najaf OB, Davachi SM, Hejazi I, Seyfi J, Khonakdar HA, Abbaspourrad A. Enhancedcompatibility of starch with poly(lactic acid) and poly(ε-caprolactone) by incorporation of POSS nanoparticles: Study on thermalproperties. Int J Biol Macromol. 2019;141:578–84.

5. Rezaei H, Seifi S, Moeinifar E, Hejazi I, Seyfi J, Khonakdar HA. Effect of nanoparticletypeand content on morphology, rheology, andcrystallinity of poly(lactic acid) using titanium dioxide and polyhedral oligomeric silsesquioxane nanoparticles. PolymCompos. 2020;41:1551–60.

6. Jia L, Tong B, Li D, Zhang W, Yang R. Crystallization and flame-retardant properties of polylactic acid composites with polyhedral octaphenyl silsesquioxane. Polym Adv Technol. 2019;30:648–65.

7. Popa MS, Frone AN, Panaitescu DM. Polyhydroxybutyrate blends: A solution for biodegradable packaging? Int J Biol Macromol. 2022;207:263–77.

8. Dandan DM, Aynali F, Doganci E, Ozkoc G. Mechanical, thermalandmorphologicalproperties of poly(lactic acid) byusing star-shapedpoly(ε-caprolactone) with POSS core. EurPolym J. 2019;121:109316.

9. Nofar M, Salehiyan R, Ciftci U, Jalali A, Durmuş A. Ductility improvements of PLA-based binary and ternary blends with controlled morphology using PBAT, PBSA, and nanoclay. Compos Part B: Eng. 2020;182:107661.

10. Frone AN, Batalu D, Chiulan I, Oprea M, Gabor AR, Nicolae CA, Raditoiu V, Trusca R, Panaitescu DM. Morpho-structural, thermal and mechanical properties of PLA/PHB/cellulose biodegradable nanocomposites obtained by compression molding, extrusion, and 3D printing. Nanomaterials. 2019;10:51.

11. Liu Z, Hu D, Huang L, Li W, Tian J, Lu L, Zhou C. Simultaneous improvement in toughness, strength and biocompatibility of poly(lactic acid) with polyhedral oligomeric silsesquioxane. ChemEng J. 2018;346:649–61.

12. Wasti S, Triggs E, Farag R, Auad M, AdhikariS BD, Li M, Ragauskas AJ. Influence of plasticizers on thermal and mechanical properties of biocomposite filaments made from lignin and polylactic acid for 3D printing. Compos Part B Eng. 2021;205:108483.

13. Shen H, Li Y, Yao W, Yang S, Yang L, Pan F, et al. Solvent-free cellulose nanocrystal fluids for simultaneous enhancement of mechanical properties, thermal conductivity, moisture permeability and antibacterial properties of polylactic acid fibrous membrane. Compos Part B Eng. 2021;222:109042.

14. Raftopoulos KN, Pielichowski K. Segmental dynamics in hybrid polymer/POSS nanomaterials. ProgPolym Sci. 2016;52:136–87.

15. Frone AN, Perrin FX, Radovici C, Panaitescu DM. Influence of branched or un-branched alkyl substitutes of POSS on morphology, thermal and mechanical properties of polyethylene. Compos Part B Eng. 2013;50:98–106.

16. Li B, Zhang Y, Wang S, Ji J. Effect of POSS on morphology and properties of poly(2,6-dimethyl-1,4-phenylene oxide)/polyamide 6 blends. EurPolym J. 2009;45:2202–10.

17. Turan D, Sirin H, Ozkoc G. Effects of POSS particles on the mechanical, thermal, and morphological properties of PLA and plasticised PLA. J ApplPolym Sci. 2011;121:1067–75.

18. Panaitescu DM, Frone AN, Radovici C, Nicolae C, Perrin FX. Influence of octyl substituted octakis(dimethylsiloxy)octasilsesquioxane on the morphology and thermal and mechanical properties of low density polyethylene. Polym Int. 2013;63:228–36.

19. Mihelčič M, Gaberšček M, Salzano de Luna M, Lavorgna M, Giuliani C, Di Carlo G, et al. Influence of silsesquioxane addition on polyurethane-based protective coatings for bronze surfaces. Appl Surf Sci. 2019;467:912–25.

20. Perrin FX, Panaitescu DM, Frone AN, Radovici C, Nicolae C. The influence of alkyl substituents of POSS in polyethylene nanocomposites. Polymer. 2013;54:2347–54.

21. Swapna VP, Abhisha VS, Stephen R. Polymer/polyhedral oligomeric silsesquioxane nanocomposite membranes for pervaporation. In: Thomas S, George SC, Jose T, editors. Polymer Nanocomposite Membranes for Pervaporation. Elsevier; 2020. p. 201–29.

22. Yilmaz S, Kodal M, Yilmaz T, Ozkoc G. Fracture toughness analysis of O-POSS/PLA composites assessed by essential work of fracture method. Compos Part B: Eng. 2014;56:527–35.

23. Blanco I, Abate L, Bottino F, Bottino P. Hepta isobutyl polyhedral oligomeric silsesquioxanes (hib-POSS). J Therm Anal Calorim. 2011;108:807–15.

24. Lu Y, Dong S, Pa Z, Liu X, Wang X. Preparation of a polylactic acid knitting mesh for pelvic floor repair and in vivo evaluation. J MechBehav Biomed Mater. 2017;74:204–13.

25. Haaparanta AM, Järvinen E, Cengiz IF, Ellä V, Kokkonen HT, Kiviranta I, Kellomäki M. Preparation and characterization of collagen/PLA, chitosan/PLA, and collagen/chitosan/PLA hybrid scaffolds for cartilage tissue engineering. J Mater Sci Mater Med. 2014;25:1129–36.

26. Jinescu G, Bacalbasa N, EvtodievA MI-A, Chiulan I, Radu ER, Frone AN, Costea R, Raita S. Perspectives of silicone elastomere implants use in preventing postoperative complications in pelvic exenteration for advanced cancers. Rev Chim. 2020;71:45–50.

27. Park S, Jung S, Heo J, Hong J. Facile synthesis of polysilsesquioxane toward durable superhydrophilic/superhydrophobic coatings for medical devices. J IndEng Chem. 2019;77:97–104.

28. Hwangbo S, Heo J, Lin X, Choi M, Hong J. Transparent superwetting nanofilms with enhanced durability at model physiological condition. Sci Rep. 2016;6:9178.

29. Chen Y, Liu S, Zhou Y, Zeng G, Liu W. Biodegradable PLA-based composites modified by POSS particles. PolymPlast Tech Mat. 2020;59:998–1009.

30. Soong SY, Cohen RE, Boyce MC, Mulliken AD. Rate-dependent deformation behavior of POSS-filled and plasticized poly(vinyl chloride). Macromolecules. 2006;39:2900–8.

31. Zhong J, Liu X, Wei D, Yan J, Wang P, Sun G, He D. Effect of incubation temperature on the self-assembly of regenerated silk fibroin: a study using AFM. Int J BiolMacromol. 2015;76:195–202.

32. Park ES, Ro HW, Nguyen CV, Jaffe RL, Yoon DY. Infrared spectroscopy study of microstructures of poly(silsesquioxane)s. Chem Mater. 2008;20:1548–54.

33. Zhang W, Yang R. Synthesis of phosphorus-containing polyhedral oligomeric Silsesquioxanes via hydrolytic condensation of a modified Silane. J ApplPolym Sci. 2011;122:3383–9.

34. Deschner T, Lønstad BT, Widenmeyer M, Anwander R. Functionalization of MCM-41 and SBA-1 with titanium(IV) (silyl)amides. J Mater Chem. 2011;21:5620–8.

35. Bianchi O, Martins JN, Luvison C, Echeverrigaray SG, Dal Castel C, Oliveira RVB (2014) Melt crystallization kinetics of polyhedral oligomeric silsesquioxane under non-isothermal conditions. J Non Cryst Solids. pp 394–395

36. Morici E, BartoloA Di, Arrigo R, Dintcheva NT. POSS grafting on polyethylene and maleic anhydride-grafted polyethylene by one-step reactive melt mixing. AdvPolym Technol. 2018;37:349–57.

37. Zhao H, She W, Shi D, Wu W, Zhang Q. Polyurethane/POSS nanocomposites for superior hydrophobicity and high ductility. Compos Part B: Eng. 2019;177:107441.

38. Bocchini S, Fukushima K, Di Blasio A, Fina A, Frache A, Geobaldo F. Polylactic acid and polylactic acid-based nanocomposite photooxidation. Biomacromol. 2010;11:2919–26.

39. El-hadi AM. Increase the elongation at break of poly (lactic acid) composites for use in food packaging films. Sci Rep. 2017;7:46767.
40. Sourkouni G, Kalogirou C, Moritz P, Gödde A, Pandis PK, Höfft O, Vouyiouka S, Zorpas AA, Argirusis C. Study on the influence of advanced treatment processes on the surface properties of polylactic acid for a bio-based circular economy for plastics. UltrasonSonochem. 2021;76:105627.
41. Pan P, Liang Z, Zhu B, Dong T, Inoue Y. Roles of physical aging on crystallization kinetics and induction period of poly(l-lactide). Macromolecules. 2008;41:8011–9.
42. Frone AN, Berlioz S, Chailan JF, Panaitescu DM. Morphology and thermal properties of PLA–cellulose nanofibers composites. CarbohydrPolym. 2013;91:377–84.
43. Baptista C, Azagury A, Baker CM, Mathiowitz E. The characterization and quantification of the induced mesophases of poly-l-lactic acid. Polym. 2021;226:123822.
44. Wang W, Jie X, Fei M, Jiang H. Synthesis of core-shell particles by batch emulsion polymerization of styrene and octavinyl polyhedral oligomeric silsesquioxane. J Polym Res. 2011;18:13–7.
45. Harris AM, Lee EC. Improving mechanical performance of injection molded PLA by controlling crystallinity. J ApplPolym Sci. 2008;107:2246–55.
46. Frone AN, Panaitescu DM, Chiulan I, Nicolae CA, Vuluga Z, Vitelaru C, Damian CM. The effect of cellulose nanofibers on the crystallinity and nanostructure of poly(lactic acid) composites. J Mater Sci. 2016;51:9771–91.
47. Xu JZ, Chen T, Yang CL, Li ZM, Mao YM, Zeng BQ, Hsiao BS. Isothermal crystallization of poly(l-lactide) induced by graphene nanosheets and carbon nanotubes: a comparative study. Macromolecules. 2010;43:5000–8.
48. Meaurio E, Lopez-Rodrıguez N, Sarasua JR. Infrared spectrum of poly(l-lactide): application to crystallinity studies. Macromolecules. 2006;9:9291–301.
49. Silverajah VSG, Ibrahim NA, Yunus WMZW, Hassan HA, Woei CB. A comparative study on the mechanical, thermal and morphological characterization of poly(lactic acid)/epoxidized palm oil blend. Int J Molec Sci. 2012;13:5878–98.
50. Liu Y, Zheng S. Inorganic-organic nanocomposites of polybenzoxazine with octa(propylglycidyl ether) polyhedral oligomeric silsesquioxane. J PolymSci Part A Polym Chem. 2006;44:1168–81.
51. Xu S, Tahon JF, De-Waele I, Stoclet G, Gaucher V. Brittle-to-ductile transition of PLA induced by macromolecular orientation. eXPRESS Polym Lett. 2020;14(11):1037–47.
52. Chen Y, Zhao L, Pan H, Jia S, Han L. Impact of d-isomer content on the microstructure and mechanical properties of uniaxially pre-stretched poly(lactic acid). Polymer. 2020;186:122022.
53. Chen Y, Han L, Chen H, Jia S, Dong L. Effect of nanoscale dispersed silica on the fabrication of microporous poly(l-lactic acid) by uniaxial stretching. Compos Part A App Sci. 2018;112:423–31.
54. Van Loock F, Fleck NA. Deformation and failure maps for PMMA in uniaxial tension. Polymer. 2018;148:259–68.
55. Arif MF, Saintier N, Meraghni F, Fitoussi J, Chemisky Y, Robert G. Multiscale fatigue damage characterization in short glass fiber reinforced polyamide-66. Comp Part B Eng. 2014;61:55–65.
56. Kim CH, Khil MS, Kim HY, Lee HU, Jahng KY. An improved hydrophilicity via electrospinning for enhanced cell attachment and proliferation. J Biomed Mater Res Part B. 2006;2006(78B):283–90.